Contents lists available at ScienceDirect

Journal of Wind Engineering and Industrial Aerodynamics

Dynamic stall in vertical axis wind turbines: Comparing experiments and computations

A-J. Buchner [a,b,*], M.W. Lohry [a], L. Martinelli [a], J. Soria [b,c], A.J. Smits [a,b]

[a] Department of Mechanical and Aerospace Engineering, Princeton University, Princeton, NJ, United States
[b] Laboratory for Turbulence Research in Aerospace and Combustion (LTRAC), Department of Mechanical and Aerospace Engineering, Monash University Melbourne, Australia
[c] Department of Aeronautical Engineering, King Abdulaziz University, Jeddah, Saudi Arabia

ARTICLE INFO

ABSTRACT

Dynamic stall is often found in unsteady aerodynamic flows where the angle of attack can vary over a large range. It is of particular interest in the context of vertical axis wind turbines, where dynamic stall is the principal impediment to achieving improved aerodynamic efficiency. Here, we report computations using the unsteady Reynolds-averaged Navier–Stokes (URANS) equations with the Menter-SST turbulence model on a two-dimensional domain, over a range of tip speed ratios typical of the operation of vertical axis wind turbines. Comparisons are made against high resolution experimental data from particle image velocimetry (PIV), with special attention to the ability of the turbulence model to emulate the turbulence properties of the flow. It is shown that the computations approximate the experimental results well in most respects.

1. Introduction

Previous studies (Sutherland et al., 2012; Ferreira et al., 2009; Buchner et al., 2014, 2015) suggest that vertical axis wind turbines can operate at power coefficients comparable to that of horizontal axis wind turbines, while reducing the unsteady interaction with the atmospheric boundary layer, providing efficient structural scaling and non-directionality with respect to the freestream wind vector, and potentially offering an increase in wind turbine array efficiency (Whittlesey et al., 2010; Dabiri, 2011; Kinzel et al., 2012). One of the principal impediments to achieving higher efficiencies is dynamic stall arising from the large and rapid changes in angle of attack that occur on each blade during the rotation cycle. Dynamic stall consists of a separation of the boundary layer from the suction-side surface of the blade and subsequent roll-up into a leading edge vortex, which can introduce excessive structural vibrations, reduce efficiency, and produce unwanted noise. Although dynamic stall is a dominating feature of vertical axis wind turbine flows, it has been studied extensively in many other contexts (McCroskey, 1976; Leishman and Beddoes, 1986; Carr, 1988; Geissler and Haselmeyer, 2006; Buchner et al., 2012; Buchner and Soria, 2014). On horizontal axis wind turbines, for example, even

mild stall decreases performance and increases noise production significantly (Hibbs, 1986; Loratro et al., 2014), and similar effects are experienced to a greater magnitude by vertical axis turbines (Allet and Paraschivoiu, 1995; Scheurich and Brown, 2011).

To predict unsteady, highly turbulent flows such as wind turbine dynamic stall requires accurate and efficient computational solvers. In many cases, especially for design purposes, unsteady Reynolds-averaged Navier–Stokes (URANS) methods are used, but turbulence models are often unreliable in predicting complex flow phenomena such as flow separation (Wilcox, 1998), and validation with experiment is crucial. In this respect, Srinivasan et al. (1995) evaluated several turbulence models for unsteady flows over an oscillating airfoil with similar dynamics to a periodically retreating helicopter rotor or a vertical axis wind turbine blade. The accuracy of force prediction in the stalled flow regime was shown to depend strongly on the turbulence model used; each of the models tested matched some aspects of the experimental force and pitching motion measurements, but none provided an accurate solution over the entire pitching cycle. Hysteresis and downstroke forces in particular were found to be poorly predicted. It was found that, of the models tested, one-equation models performed better than algebraic models such as Baldwin–Lomax (Baldwin and Lomax, 1978) or the renormalisation group theory method (Yakhot and Orzag, 1986). Similarly, McLaren (2011) and McLaren et al. (2012) performed URANS on a high solidity vertical axis wind turbine but only validated blade forces against the experimental data of Sheldahl and Klimas (1981) for a stationary airfoil. Their

Nomenclature

A	cross-sectional area of turbine	$\overline{U}$	resolved scale velocity
c	chord length of turbine blades	$\hat{u}$	subgrid scale velocity
C_f	coefficient of friction	$u, v, w, u_{i,j}$	velocity components
C_p	coefficient of power	$x, y, z, x_{i,j}$	coordinate variables
C_p	specific heat capacity	$\mathbf{w}$	vector of flow variables, $[\rho, \rho u, \rho v, \rho E]$
C_s	Smagorinsky constant	α_{s0}	laminar separation bubble formation angle
E	energy	α_{s1}	dynamic stall vortex formation angle
i	iteration number	γ	ratio of specific heats
i, j	tensor subscripts	Γ	circulation
k	turbulent kinetic energy	δ	uncertainty
L	integral length scale	Δ_{IW}	PIV vector spacing, or resolution
n	number of blades	ϵ	turbulent dissipation rate
Pr	Prandtl number	θ	azimuthal blade angle
Pr_t	turbulent Prandtl number	λ	tip speed ratio
R	radius of vertical axis turbine	ν	kinematic viscosity
$\mathbf{R}$	residual vector	ν_t	kinematic eddy viscosity
Re_b	blade Reynolds number	ρ	density
Re_t	turbine Reynolds number	ρ_{xx}	cross correlation coefficient
$\overline{S}$	resolved scale rate of strain tensor	σ	solidity ratio
t	time	$\overline{\tau}$	azimuthally averaged rotor torque
$\tilde{t}$	pseudo-time	τ	subgrid scale stress
U_∞	freestream velocity	ω	specific turbulent dissipation rate
		ω_z	spanwise vorticity component
		Ω	rotation speed of vertical axis turbine

results suggested that beyond stall the force predictions provided by the standard Wilcox k–ω (Wilcox, 1988, 1998) and Menter shear stress transport (SST) (Menter, 1993, 1994) models are superior to the k–ϵ model (Jones and Launder, 1972).

A more complete validation was given by Ferreira et al. (2010), who compared several different turbulence models against two-dimensional experimental velocity data, but only at a single tip speed ratio ($\lambda = 2$). They found that both Spalart–Allmaras (Spalart and Allmaras, 1992, 1994) and k–ϵ turbulence models under-predicted leading edge circulation production and were unable to match the trailing edge wake roll-up behaviour observed in the experiments. Better agreement was only achieved by resorting to more computationally intensive Large Eddy Simulation (LES) and Detached Eddy Simulation (DES) methods. In none of these prior publications has there been discussion of the distribution and quantitative accuracy of the modelled turbulent flow properties and their effect on the mean behaviour of the velocity field. To fill this need, we present new comparisons of URANS with experiment in the context of dynamic stall on vertical axis wind turbines, and we provide direct comparisons between unsteady flow fields, as well examining the unsteady vortex shedding behaviour.

2. Numerical method

The time dependent flow around the vertical axis wind turbine configuration is modelled by the unsteady, compressible Reynolds-averaged Navier–Stokes equations. A two-equation Menter shear stress transport (SST) model (Menter, 1993, 1994, 2009) is used for closure, with equations for the turbulent kinetic energy and specific dissipation rate. The strain rate is used as the turbulence production term and no wall functions are used. The Menter-SST model has previously been shown (Bardina et al., 1997; McLaren, 2011; McLaren et al., 2012) to produce results in separated or adverse pressure gradient flows of superior accuracy to simulations using a standard Wilcox k–ω or Launder and Sharma k–ϵ model.

The flow equations are solved in integral form by second order accurate finite volume discretisation in space on hexahedral cells. A fully implicit dual-time stepping scheme based on a second order A-stable backward differentiation formula (BDF) is used where the inner iteration is converged by an efficient multigrid time-stepping scheme (Jameson, 1991). Methods of this class combine the stability and time-step advantages of fully implicit schemes while allowing an efficient implementation on parallel machines (Alonso et al., 1995; Jameson and Martinelli, 1998). This approach also allows for time-accurate extension for low Mach number flow using a preconditioner (Belov et al., 1997).

A multi-block structured mesh approach has been selected for this work, which allows for accurate representation of the boundary layers near the blades. The original implementation was developed by Martinelli et al. (1997) and Reuther et al. (1997) as *FLO107MB* and has been widely used and validated for a wide range of flow regimes. For this study, we used the multi-block *SUmb* solver appropriately modified to include the low Mach number preconditioner of Weiss and Smith (1995). *SUmb* was developed at Stanford University by van der Weide et al. (2006), and evolved from *FLO107MB*.

The computations were performed on a structured multi-domain grid with a circular boundary, centred on the turbine axis and extending radially to 10 turbine diameters, or 75 blade chord lengths (Fig. 1). The two-dimensional mesh allows for a relatively small number of cells $\sim \mathcal{O}(10^5)$, which is shown here to be sufficient to capture the main features of the unsteady separating flow. The first wall-normal grid point location at the turbine blades is at $y^+ = 1$ for a Reynolds number based on the freestream velocity and chord length, and the grid is expanded at a rate away from the wall of 1.09 using the hyperbolic tangent stretching function of Vinokur (1983). The simulation is run with a time-step size equal to 2.5 degrees of rotation of the turbine, equivalent to 0.15 blade convection times $c/\lambda U_\infty$, and the solution is judged converged after four periods of rotation, when the period to period root mean square error of the force and moment histories drops below 2.5% of the maximum value. A freestream turbulence intensity of 1%, typical of wind tunnels, is applied to the numerical
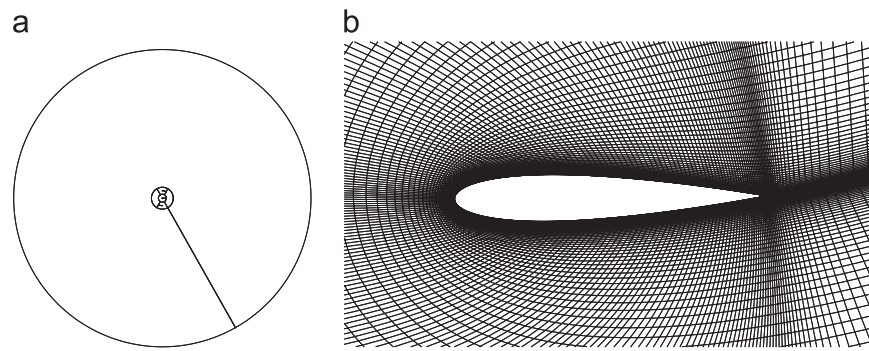
a b

Fig. 1. Computational mesh. (a) Whole computational domain, illustrating sub-domain boundaries. (b) Structured grid arrangement in near field of turbine blade.
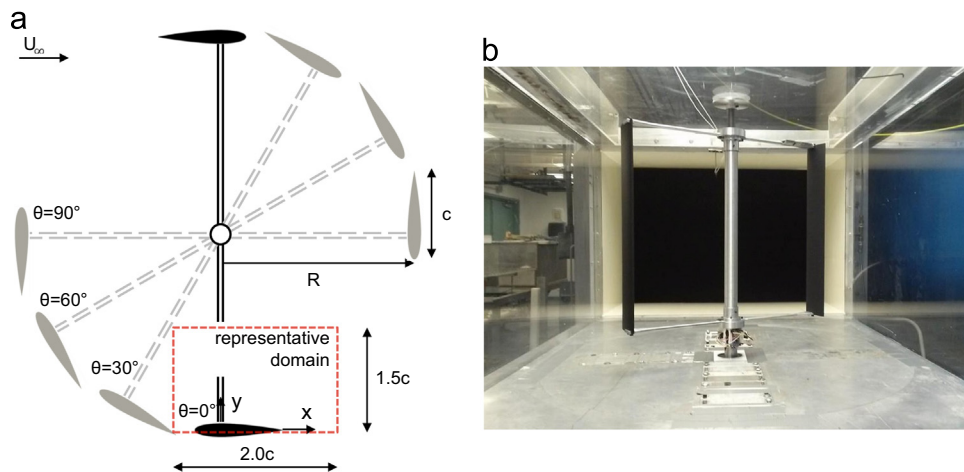
a b

Fig. 2. Experimental setup in the wind tunnel, with representative domain and key geometry marked.

solution, and the ratio of the eddy viscosity to kinematic viscosity $\nu_t/\nu = 0.01$ in the freestream. Computations were performed on a small cluster, requiring approximately 1 h wall-clock time per revolution on a 16-core AMD 6274 processor.

A grid convergence study was also performed by doubling the spatial resolution to check for numerical grid independence. The solutions rendered by these higher resolution simulations differed only marginally from the lower resolution simulations, with an approximately 97.5% correlation between the solutions and an average disparity between the velocity fields of less than 5% of the freestream velocity. No clear qualitative or quantitative spatio-temporal topological differences between the solutions were observed, with no greater detail in the detached stall structures being resolved by the finer grid. The lower resolution numerical grid can therefore be considered sufficiently resolved for the current study.

3. Description of the experiment

To compare with the simulations, a vertical axis wind turbine model was tested in a wind tunnel under the same flow conditions, and stereoscopic particle image velocimetry (SPIV) was used to measure the unsteady flow fields over the blades. The turbine had two 450 mm span aluminium turbine blades ($n=2$), each of chord length $c = 75$ mm. A two-bladed design was used to minimise solidity and blade–blade interactions whilst permitting a sufficiently large chord length to allow highly resolved PIV measurements of the leading edge flow separation. The solidity ratio for the experiment was held constant at $\sigma = nc/2R = 0.3$, where R is the radius of the turbine. The test section of the wind tunnel

measured 2×3 ft (0.61×0.915 m); the arrangement is shown in Fig. 2, and the experimental conditions are summarised in Table 1. Here, the freestream velocity is U_∞, the turbine's angular velocity is Ω, the tip speed ratio $\lambda = R\Omega/U_\infty$, the turbine Reynolds number $Re_t = 2RU_\infty/\nu$, and the blade Reynolds number is $Re_b = cR\Omega/\nu$, where ν is the kinematic viscosity. The blade-scaled Reynolds number, $Re_b = 70,000$, was chosen to match the work of Ferreira et al. (2009), and it was held constant over all experiments and computations ($\Omega = 60$ rad/s). The turbine Reynolds number varies in this experiment as a function of tip speed ratio, as shown.

Digital stereoscopic PIV measurements (Willert and Gharib, 1991; Arroyo and Greated, 1991; Keane and Adrian, 1992; Prasad, 2000; Raffel et al., 2007) were performed at the spanwise mid-plane of the experiment, using two 2560×2160 pixel sCMOS double shutter cameras placed at an included angle between $60°$ and $90°$, suspended on a turntable above the test section. A two-plane Soloff mapping (Soloff et al., 1997) was performed to calibrate between camera views. The strongest flow separation event during the motion of the turbine blades occurs during the upwind passage of each blade. Phase-locked PIV measurements were taken over the radially inwards-facing surface of the turbine blades at a range of azimuthal positions (Table 1), capturing each stage of the dynamic flow separation and stall. The measurement domain was governed by the region of common field of view to both cameras and measured approximately 150×125 mm. Each pixel measured 6.5 μm on each side, and the magnification was approximately 9.0. Fig. 2 illustrates the experimental arrangement, and shows a representative PIV measurement domain.

Image acquisition was phase-locked with the rotation of the turbine, using an optical encoder and Arduino nano v3.3 for timing and acquisition control. Phase-locking accuracy was found to be

Table 1
Experimental conditions.

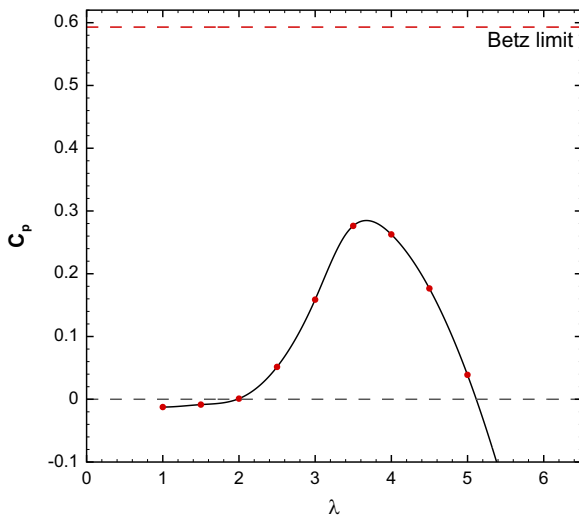| λ	U_∞ (m/s)	Re_t	θ_{range} (deg)	$\theta_{increment}$ (deg)
1	15	466,700	30–105	15
2	7.5	233,400	30–135	15
3	5	155,600	30–135	15

Fig. 3. Power coefficient variation with tip speed ratio, from URANS simulations of a two-blade H-rotor vertical axis wind turbine at Reynolds number $Re_b = 70,000$.

within 0.5°, or approximately 2.9% of the blade chord length. A 1000 image pair ensemble was acquired at each measurement condition and azimuthal phase and the minimum intensity across each ensemble was subtracted to remove biases from background reflections. A high-pass filter spatially equalised image intensities over the measurement domain. A multigrid cross-correlation (Soria, 1996) was performed, iterating from 64×64 pixels to a final interrogation window size of 24×24 pixels. The final spatial resolution of the SPIV measurement was approximately 0.7 mm or $0.0093c$ per vector. A maximum displacement limit, and normalised local median filter (Westerweel and Scarano, 2005), were applied to the cross-correlation results, with rejected vectors interpolated from their nearest neighbours.

4. Results

4.1. Power curve

To characterise the performance of the turbine used in this study, the computed power coefficient as a function of tip speed ratio is presented in Fig. 3 for $\lambda = 1$ to 5. The power coefficient is defined as

$$C_p = \frac{\overline{\tau}\Omega}{\frac{1}{2}\rho A U_\infty^3} \tag{1}$$

where $\overline{\tau}$ is the azimuthally averaged rotor torque, and A denotes the frontal area of the turbine, equal to the height times the rotor diameter. The turbine does not produce net power below a tip speed ratio of $\lambda = 2$, and reaches a maximum power coefficient of $C_p \approx 0.3$ at $\lambda \approx 3.5 - 4.0$, coinciding with the higher end of the tip speed ratio range for which dynamic stall occurs. At higher tip speed ratios, $\lambda \gtrsim 4$, the efficiency of the turbine decreases rapidly

because, even though stall is weak at high tip speed ratios, the blade angle of attack is also reduced. These calculations confirm that the operation of the turbine is dominated by large scale dynamic flow separation over the tip speed ratio range chosen for the experiment.

4.2. Mean stall topology

Fig. 4 illustrates the level of agreement that the URANS simulation provides in terms of the mean stall topology observed in the experiments. Three example velocity fields are shown, at an azimuthal phase of 90° and at tip speed ratios of $\lambda = 1$, 2 and 3, and they will be used throughout this section to compare the experimental and numerical results. These fields are representative of distinct phases of the stall phenomenon. In the $\lambda = 3$ case, the stall has not yet developed at $\theta = 90°$, with only a small region of reversed flow near the trailing edge. At $\lambda = 2$, leading edge separation has occurred and a dynamic stall vortex exists, while at $\lambda = 1$ the leading edge dynamic stall vortex has begun to convect away from the blade and a trailing edge vortex has already been formed at $\theta = 90°$. These features are all reproduced well in the simulation.

Where the numerical results differ from the experiment most is in the surface separation characteristics of the boundary layer aft of the main dynamic stall vortex, as illustrated in Fig. 4(b). In addition, the vorticity fields are more diffuse in the numerical simulation. This feature is especially noticeable in contrasting the experimental data in Fig. 4(a), bottom with the CFD data shown in Fig. 4(a), top. In the experiment, the leading edge vortex and the shear layer connecting it to the leading edge are well defined, and the regions of rotational and irrotational flow are sharply delineated, whereas in the computation the vorticity is diffuse and the shear layer is not clear. This comparison suggests a high dissipation rate in the numerical results. Furthermore, the vorticity in the core of the trailing edge vortex appears more concentrated in the CFD results than in data from experiment. This is a consequence of variability in the location of the vortex core from measurement to measurement, an effect which the more deterministic CFD does not predict. The total circulation in the trailing edge vortex for the PIV and CFD match well, and thus this discrepancy should not unduly affect the determination of forces.

Despite the good agreement between the numerics and experiment regarding the upper surface separation point prior to stall (Fig. 6), once the dynamic stall vortex forms the behaviour of the separated upper-surface shear layer diverges between the numerics and experiment. While the experiments suggest that the boundary layer aft of the developing leading edge vortex remains relatively undisturbed as it convects downstream past the trailing edge, the numerical simulation indicates that the boundary layer instead should roll up into a vortex of similar dimensions to the leading edge vortex. The reason for this discrepancy is uncertain. However, the phenomenon has some basis in reality as it has been observed in experiments also (Fig. 5), although under different conditions than those at which it is observed in the computations.

To quantitatively illustrate the discrepancy between URANS and PIV results, the absolute difference between the computational and experimental velocity fields is averaged over the measurement domain for the conditions where PIV measurements were available (Fig. 7(a)). The average discrepancy between computation and experiment is 5–10%, with the greatest errors observed in the part of the rotational cycle corresponding to massive flow separation.

A cross-correlation was also performed between velocity fields obtained from URANS and PIV, for all phases at which both sets of data were available, to provide another quantitative measure of the comparison. The cross-correlation coefficient, ρ_{xx}, is
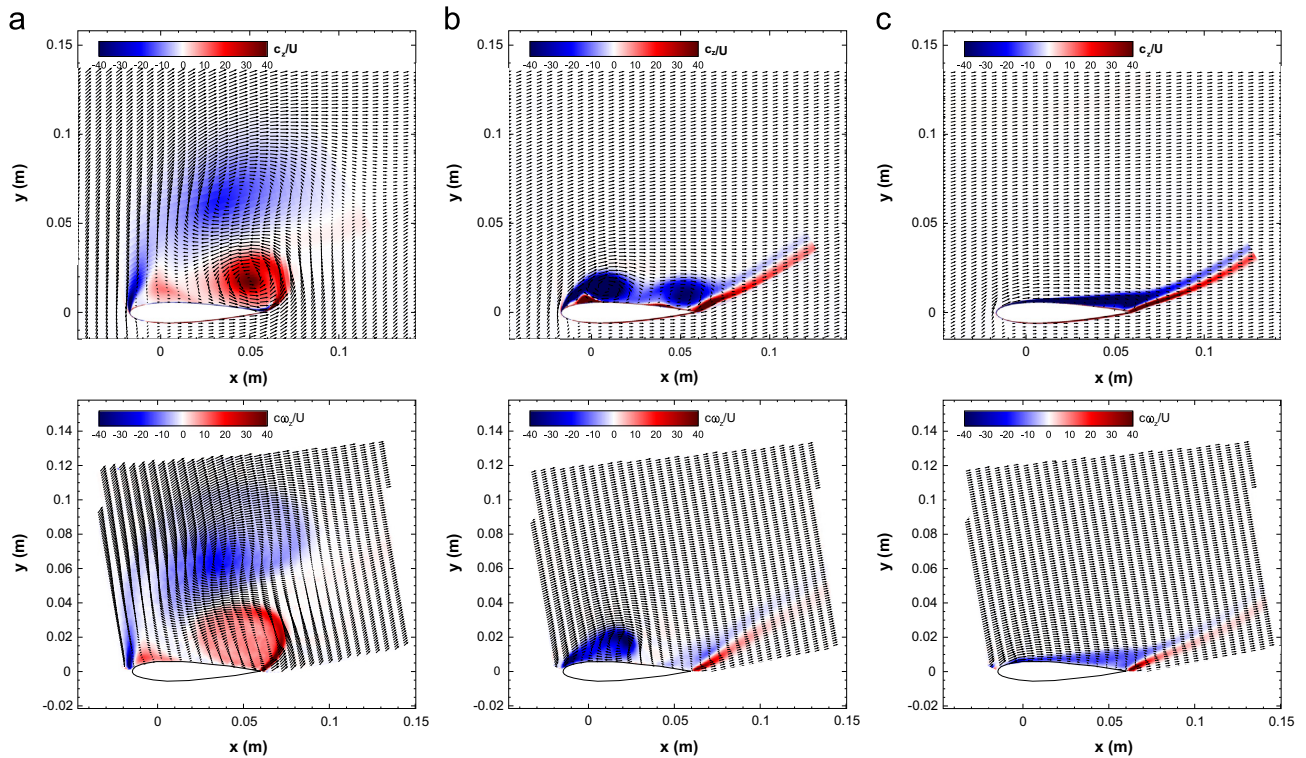
167

Fig. 4. Vorticity fields from URANS simulation (top) and SPIV experiment (bottom) at $\theta = 90°$. (a) $\lambda = 1$, (b) $\lambda = 2$, and (c) $\lambda = 3$.
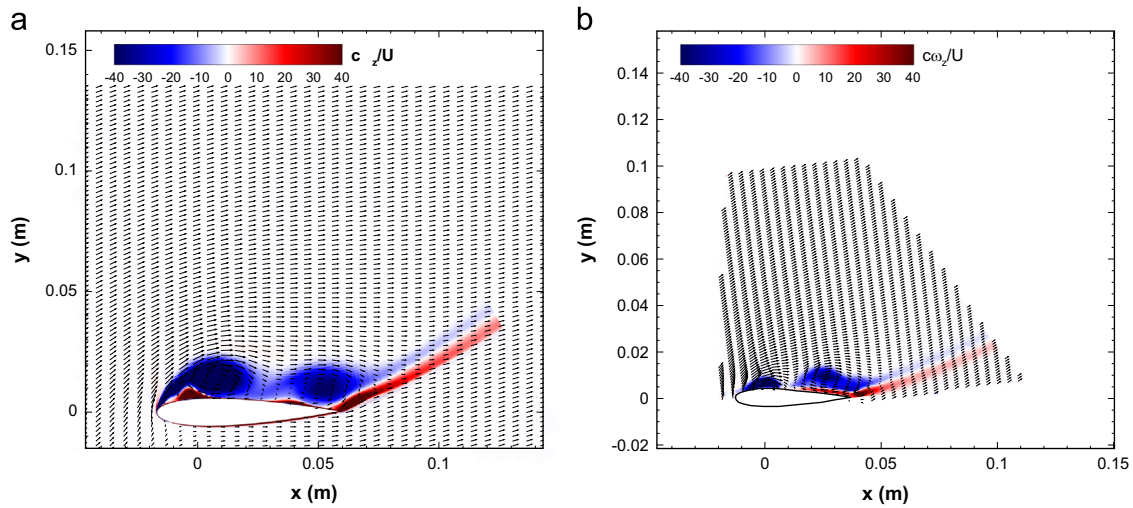

Fig. 5. Anomalous upper surface vortex shedding behaviour. URANS, $\lambda = 2$, $c = 75$ mm, $\theta = 90°$ (at left) and from PIV, $\lambda = 1$, $c = 50$ mm, $\theta = 45°$ (at right).

normalised by the square root of the product of the standard deviation of each velocity field, such that the value of the resulting correlation coefficient lies in the range $-1 \leq \rho_{xx} \leq 1$. The values of ρ_{xx} are shown as a function of azimuthal blade angle in Fig. 7(b). A value closer to 1 implies greater agreement. In the unseparated regime the cross-correlation is 0.97–0.99, with values declining for the fluctuating flow once massive separation has occurred. Even under deep dynamic stall conditions, correlation between the computation and the experimental results remains consistently above 0.75.

4.3. Flow separation angle and shedding of circulation

The azimuthal angle at which the suction surface boundary layer separates and subsequently rolls up into a dynamic stall

vortex is defined by the first appearance of an accumulation of vorticity at the leading edge of thickness significantly greater than the surrounding boundary layer. This angle is denoted α_{s1} and it is shown in Fig. 8 for both URANS and PIV results. Error bars represent the uncertainty due to finite azimuthal angular resolution. The simulations match the experiments within the angular uncertainty of the measurement, albeit with an apparent small bias towards late separation. At the highest tip speed ratio considered, $\lambda = 3$, this bias lies just outside the measurement uncertainty. The angle α_{s0} plotted in Fig. 8 denotes the angle at which the first sign of a separation bubble appears in the URANS results. These values are obtained by noting the first indication of leading edge flow reversal at the blade surface. We see that there is a significant azimuthal angle traversed by the blade during the delay between the first leading edge flow reversal and the appearance

and rapid growth of a coherent leading edge vortex structure, implying a strongly stable laminar separation bubble.

The circulation shed from the leading edge is given in Fig. 9. Excellent agreement between computation and experiment is seen at low tip speed ratios, especially at $\lambda = 2$, but there is a significant bias in the data for $\lambda = 3$. At this tip speed ratio, the rate of circulation production is not significantly different between computation and experiment, but rather there is a delay in azimuthal angle at which the circulation shedding starts that causes the bias error in the circulation values from the computation. This observation is consistent with the delayed stall angle seen at $\lambda = 3$ in Fig. 8. The circulation values at $\lambda = 2$ were calculated exclusive of the anomalous second vortex formed in the numerical simulation (Fig. 4(b)), and since the computational and experimental values match, it appears that this anomalous vortex is composed of vorticity from the boundary layer aft of the dynamic stall vortex and does not have its origin in the leading edge separation.

4.4. Turbulence properties

The spatial distributions of turbulent kinetic energy, k, normalised by U_∞, are illustrated in Fig. 10. Although stereoscopic
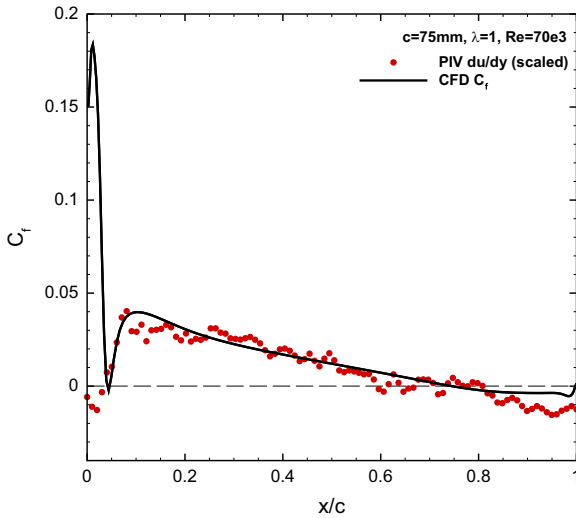

Fig. 6. Blade surface skin friction coefficient and scaled wall-normal velocity gradient for $\lambda = 1$, coinciding with initial flow reversal near the leading edge.

PIV yields three-component velocity data, for direct comparison with the 2D URANS simulation only two components of the experimental velocity field were used to calculate the turbulent kinetic energy, with a correction assuming isotropy. It was found that very little difference ($|k_{2D} - k_{3D}|/U_\infty^2 \approx \mathcal{O}(10^{-3})$) exists between the two-component and the three-component experimental turbulent kinetic energy with respect to spatio-temporal distribution or magnitude.

Similar turbulent kinetic energy distributions are seen in URANS and PIV data, but with several important differences. Prior to dynamic stall vortex formation (Fig. 10(c)), the experiment and computation agree well. However, significant differences appear over the blade suction surface once the leading edge stalls (Fig. 10(b)), reflecting the differences in topology demonstrated by the $\lambda = 2$ case at $\theta = 90°$ (Fig. 4(b)). In the later stages of dynamic stall, as presented by the example shown in Fig. 10(a), k is significantly underestimated in the core of both the leading and trailing edge vortices. This result is another manifestation of the inability of the simulation to capture the vortex locational variability and meandering seen in the experiment. Variability in the measured location of the tight vortex core at $\lambda = 2$ in Fig. 10(b) also accounts for the much higher turbulent fluctuations measured in that region, when compared to the numerical analysis.

In Section 4.2, it was noted that when considering the mean stall topology the numerical simulation appears too dissipative. There are several methods by which we can directly calculate the turbulent dissipation rate, ϵ, from experimental data. Direct calculation from the rate of strain tensor is possible, if one assumes turbulent isotropy, but likely to be inaccurate due to the insufficient spatial resolution of the PIV data, which also limits the accuracy of estimating the dissipation from spatial correlations like structure functions. Another method involves balancing the equation for the turbulent kinetic energy, but this approach requires estimating the pressure–velocity correlation, and extracting the pressure field from PIV data remains a difficult problem (Charonko et al., 2010; van Oudheusden, 2013). Alternatively, the turbulent dissipation rate may be calculated from the spectrum, but this requires that the turbulence is homogeneous, an assumption which cannot be made for the present, highly inhomogeneous flow.

Instead, we estimate the turbulent dissipation rate from PIV using the method proposed by Sheng et al. (2000) involving a large eddy type approach. If the true properties of the flow are composed of a component resolved by the PIV measurement, $\overline{U}_i$,
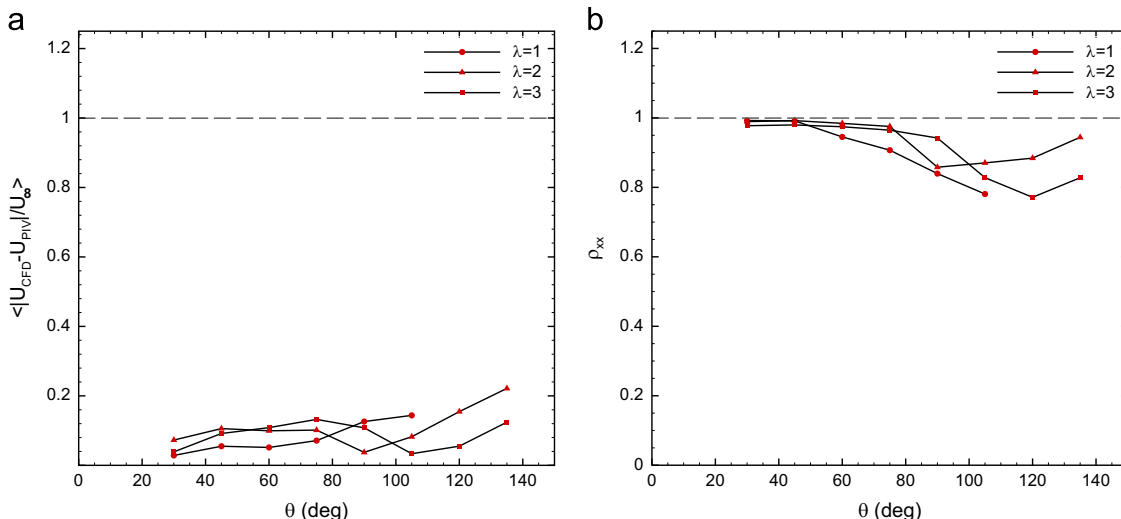

Fig. 7. Quantitative comparison between URANS and PIV velocity fields. Experimental-numerical deviation, normalised by freestream velocity (a), and cross-correlation coefficient between numerical and experimental results (b).
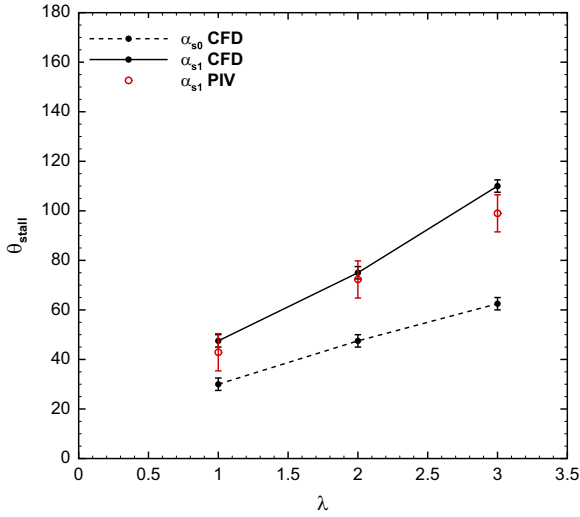
Fig. 8. Stall angle comparison, showing angle of initial separation bubble formation, α_{s0}, and angle of rapid expansion of leading edge vortex, α_{s1}, for PIV and URANS.
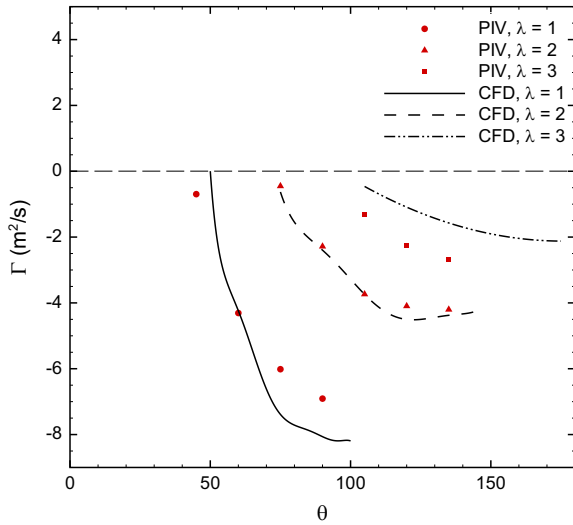

Fig. 9. Circulation production at leading edge of blade as a function of azimuthal angle and tip speed ratio.

and a component unresolved by PIV, $\hat{u}_i$, the true velocity u_i may be written as $u_i = \overline{U}_i + \hat{u}_i$. Following the usual decompositions used in Large Eddy Simulations (need reference) the dissipation rate is then given approximately by

$$\epsilon \approx -2\left\langle \tau_{ij}\overline{S}_{ij} \right\rangle \tag{2}$$

where $\overline{S}_{ij}$ is the rate of strain tensor measured by PIV. The subgrid scale stress, τ_{ij}, is unknown and must be modelled. Here we use the well-known eddy viscosity model by Smagorinsky (1963)

$$\tau_{ij} = -C_s^2\Delta_{IW}^2|\overline{S}|\overline{S}_{ij} \tag{3}$$

where Δ_{IW} is the PIV vector spacing, and C_s is the Smagorinsky constant taken to be equal to 0.17. To compare directly with the two-dimensional URANS simulation's modelled dissipation rate, the dissipation rate calculated from PIV measurements is based on only the two-dimensional components of the rate of strain tensor.

Fig. 11 illustrates the spatial distribution of turbulent dissipation rate for the three example cases used throughout this paper.

The turbulent dissipation values resulting from the method of Sheng et al. (2000) appear to be of the same magnitude as those obtained from the URANS computation. A similar distribution was rendered by the homogeneous estimate $\epsilon = k^{3/2}/L$, and assuming that the integral length scale $L=c$.

Regions of high turbulent dissipation are seen to be associated primarily with regions of high shear. Prior to dynamic stall this means high dissipation near the trailing edge, around the point on the blade's upper surface where flow reversal starts, and in the shear layer flowing downstream from this point. Similarly, and unsurprisingly, regions of high shear near the leading and trailing edge post-stall also exhibit high dissipation. Consistent with the mean topology and turbulent kinetic energy results, the high dissipation in the vortex cores is not captured by the numerical simulation as it is primarily a result of large-scale variability of the vortex core location from instance to instance in the real flow. Generally, the URANS results display a consistent bias towards a more dissipative nature, accounting for the more diffuse appearance of the leading edge vortex in Fig. 4(a).

4.5. Experimental uncertainty analysis

The uncertainty in determining the peak cross-correlation location in PIV is typically on the order of 0.1 pixels (Raffel et al., 2007). In the current experiment, this particle displacement uncertainty is equivalent to between 2.9 and 4.4% of the freestream velocity, U_∞. Given an ensemble of 1000 image pairs, the uncertainty in the mean velocity is of the order 0.09–0.14% of U_∞.

The estimation of differential quantities and vorticity from PIV data is biased, dependent on the spatial resolution of the velocity data relative to the length scale of the vortex (Fouras and Soria, 1998). The current measurement is sufficiently resolved such that the underestimation of vorticity in the primary dynamic stall structures is vanishingly small, with a maximum in the shear layer near the leading edge of $\omega_{z_{bias}}/\omega_z \approx 0.0015$. This vorticity bias is sufficiently small that it may be neglected in calculating the circulation in the leading edge dynamic stall vortex. Likewise, the effect of random velocity errors may be neglected for integral quantities such as circulation.

Turbulent kinetic energy values calculated from PIV data are typically overestimated due to random velocity error. We find that the turbulent kinetic energy calculated in the current experiment is on the order of $\delta(k)/U_\infty^2 = 0.0075$ higher than the true value, which is consistent with values of $k/U_\infty = 0.001$ to 0.0065 measured in the irrotational regions of the flow, where the error term is dominant.

5. Conclusions

In general, the agreement between the URANS computation and SPIV experiment is encouraging, especially considering the low-to-moderate Reynolds number, a flow regime which is well known to be problematic for turbulence models in general (Wilcox, 1998; Rumsey, 2007; Rumsey and Spalart, 2008). The evolution of the dynamic stall vortex system as it arises over a range of tip speed ratios in the computation agrees well with the experimental data from the pre-stall regime right through to late stall. The discrepancies in the mean flow behaviour are generally restricted to less than 10% of the freestream value. Stall angle and production of circulation are well modelled by the URANS simulation, but with some evidence of slightly delayed flow separation at the highest tip speed ratio tested.

Despite these promising observations, the Menter-SST turbulence model implemented here was found to be too dissipative,
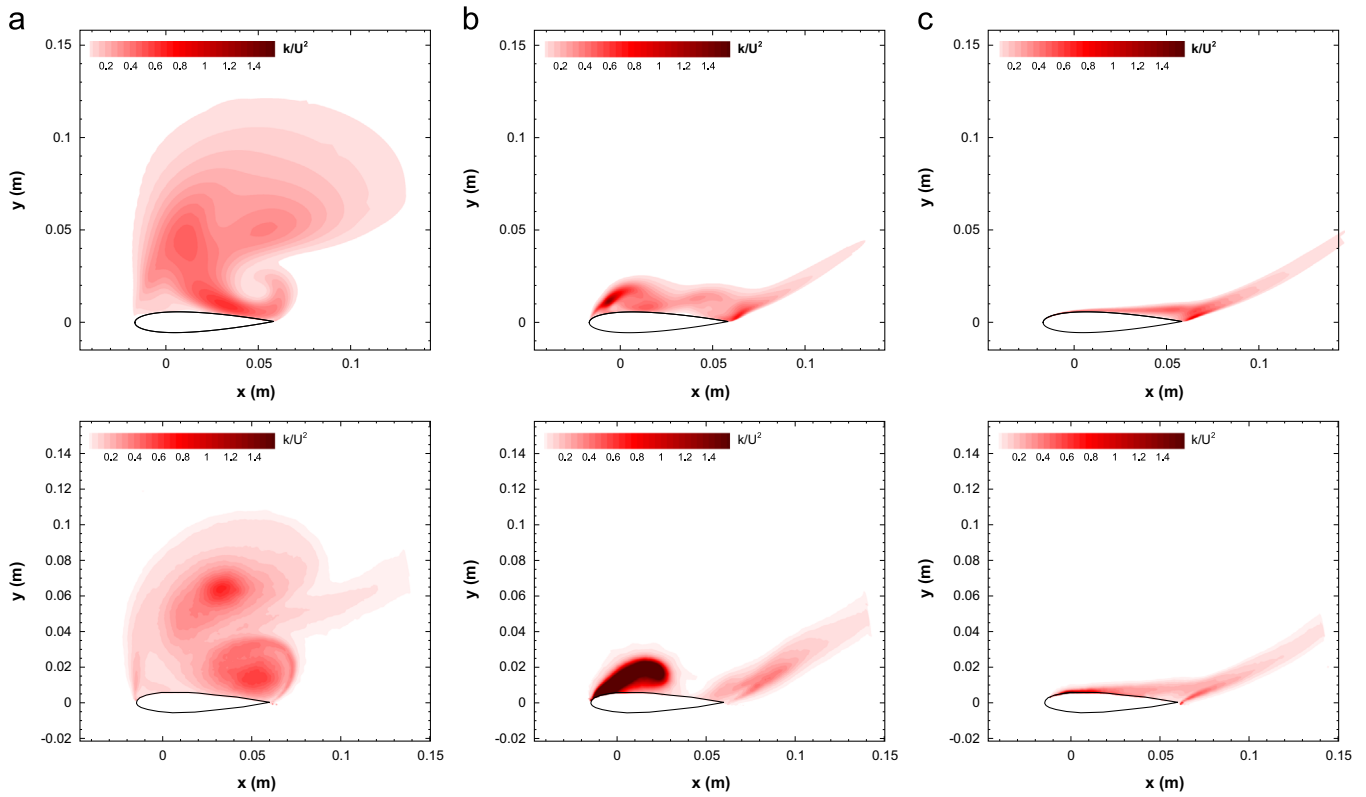
Fig. 10. TKE fields from URANS simulation (top) and SPIV experiment (bottom) at $\theta = 90°$. (a) $\lambda = 1$, (b) $\lambda = 2$, and (c) $\lambda = 3$.
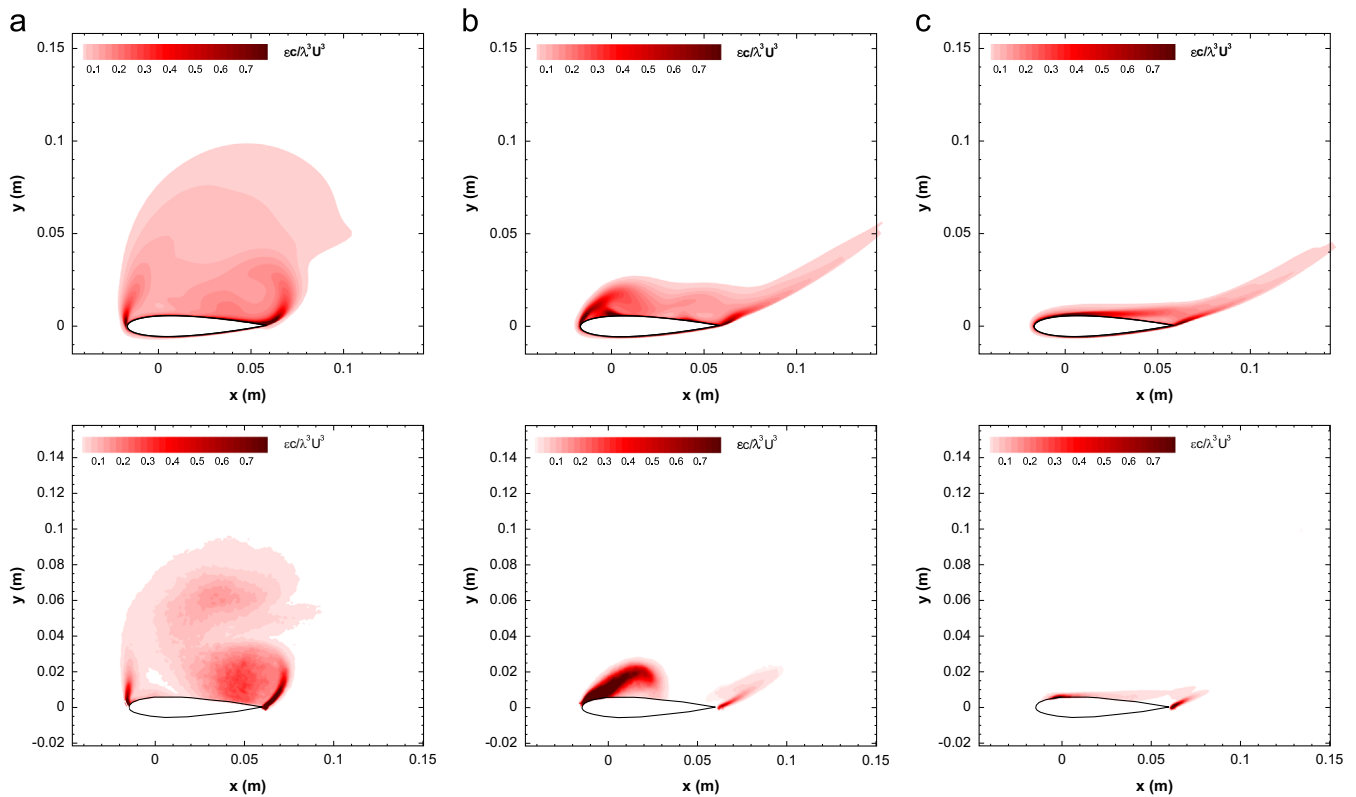

Fig. 11. Dissipation rate, ϵ, fields from URANS simulation (top) and SPIV experiment (bottom) at $\theta = 90°$. (a) $\lambda = 1$, (b) $\lambda = 2$, and (c) $\lambda = 3$.

and failed to account for large-scale variability in the vortex dynamics evident from the experiment. Nevertheless, it has been shown that unsteady RANS calculations, using well established techniques of sufficient computational efficiency for wind turbine design applications, can give consistent and accurate predictions of dynamic stall within the error estimates quantified here.

Acknowledgements

References

Allet, A., Paraschivoiu, I., 1995. Viscous flow and dynamic stall effects on vertical-axis wind turbines. Int. J. Rotating Mach. 2 (1), 1–14.

Alonso, J.J., Martinelli, L., Jameson, A., 1995. Multigrid unsteady Navier–Stokes calculations with aeroelastic applications. In: The 33rd AIAA Aerospace Sciences Meeting and Exhibit, January 9–12, Reno, NV. AIAA95-0048.

Arroyo, M.P., Greated, C.A., 1991. Stereoscopic particle image velocimetry. Meas. Sci. Technol. 2 (12), 1181–1186.

Baldwin, B.S., Lomax, H., 1978. Thin layer approximation and algebraic model for separated turbulent flows. In: The 16th AIAA Aerospace Sciences Meeting, Huntsville, AL, January 16–18, AIAA78-0257.

Bardina, J.E., Huang, P.G., Coakley, T.J., 1997. Turbulence Modeling Validation, Testing, and Development. NASA Technical Memorandum 110446.

Belov, A., Martinelli, L., Jameson, A., 1997. Three-dimensional unsteady incompressible flow computations using multigrid. In: The 35th AIAA Aerospace Sciences Meeting and Exhibit, Reno NV, AIAA97-0443.

Buchner, A-J., Soria, J., 2014. Measurements of the flow due to a rapidly pitching plate using time resolved high resolution piv. Aerosp. Sci. Technol. 44, 4–17 (Special issue: Instability and Control of Massively Separated Flows).

Buchner, A.-J., Buchmann, N.A., Kilany, K., Atkinson, C.H., Soria, J., 2012. Stereoscopic and tomographic piv of a pitching plate. Exp. Fluids 52, 299–314.

Buchner, A-J., Smits, A.J., Soria, J., 2014. Scaling of vertical axis wind turbine dynamic stall. In: The 19th Australasian Fluid Mechanics Conference, Melbourne, Australia.

Buchner, A-J., Soria, J., Smits, A.J., 2015. Circulation production and shedding from vertical axis wind turbine blades undergoing dynamic stall. In: The Ninth International Symposium on Turbulence and Shear Flow Phenomena, Melbourne, Australia.

Carr, L.W., 1988. Progress in analysis and prediction of dynamic stall. J. Aircr. 25 (1), 6–17.

Charonko, J.J., King, C.V., Smith, B.L., Vlachos, P.P., 2010. Assessment of pressure field calculations from particle image velocimetry measurements. Meas. Sci. Technol. 21 (10).

Dabiri, J.O., 2011. Potential order-of-magnitude enhancement of wind farm power density via counter-rotating vertical axis wind turbine arrays. J. Renew. Sustain. Energy 3.

Ferreira, C.S., van Kuik, G., van Bussel, G., Scarano, F., 2009. Visualisation by piv of dynamic stall on a vertical axis wind turbine. Exp. Fluids 46, 97–108.

Ferreira, C.S., van Zuijlen, A., Bijl, H., van Bussel, G., van Kuik, G., 2010. Simulating dynamic stall in a two-dimensional vertical axis wind turbine: verification and validation with particle image velocimetry data. Wind Energy 13, 1–17.

Fouras, A., Soria, J., 1998. Accuracy of out-of-plane vorticity measurements derived from in-plane velocity field data. Exp. Fluids 25, 409–430.

Geissler, W., Haselmeyer, H., 2006. Investigation of dynamic stall onset. Aerosp. Sci. Technol. 10 (7), 590–600.

Hibbs, B.D., 1986. Hawt Performance with Dynamic Stall. SERI/STR 217-2732.

Jameson, A., 1991. Time Dependent Calculations Using Multigrid, with Applications to Unsteady Flows Past Air Foils and Wings. AIAA Paper 91-1596.

Jameson, A., Martinelli, L., 1998. Mesh refinement and modelling errors in flow simulation. AIAA J. 36 (5), 676–686.

Jones, W.P., Launder, B.E., 1972. The prediction of laminarization with a two-equation model of turbulence. Int. J. Heat Mass Transf. 15, 301–314.

Keane, R.D., Adrian, R.J., 1992. Theory of cross-correlation analysis of piv images. Appl. Sci. Res. 49 (3), 191–215.

Kinzel, M., Mulligan, Q., Dabiri, J.O., 2012. Energy exchange in an array of vertical axis wind turbines. J. Turbul. 13 (38), 1–13.

Leishman, J.G., Beddoes, T.S., 1986. A semi-empirical model for dynamic stall. J. Am. Helicopter Soc. 34, 3–17.

Loratro, A., Arjomandi, M., Kelso, R., Cazzolato, B., 2014. A discussion of wind turbine interaction and stall contributions to wind farm noise. J. Wind Eng. Ind. Aerodyn. 127, 1–10.

Martinelli, L., Alonso, J.J., Jameson, A., Reuther, J., 1997. Cfd analysis and design optimization using parallel computers. In: Bhanot, G., Chen, S., Seiden, P. (Eds.), Some New Directions in Science on Computers. World Scientific Pub Co, London, pp. 3–40.

McCroskey, W.J., Carr, L.W., McAlister, K.W., 1976. Dynamic stall experiments on oscillating airfoils. AIAA J. 14 (1).

McLaren, K., 2011. A Numerical and Experimental Study of Unsteady Loading of High Solidity Vertical Axis Wind Turbines (Ph.D. thesis). McMaster University.

McLaren, K., Tullis, S., Ziada, S., 2012. Computational fluid dynamics simulation of the aerodynamics of a high solidity, small-scale vertical axis wind turbine. Wind Energy 15, 349–361.

Menter, F.R., 1993. Zonal two equation k–ω turbulence models for aerodynamic flows. In: The 24th AIAA Fluid Dynamics Conference, Orlando, FL. AIAA Paper 93-2906.

Menter, F.R., 1994. Two-equation eddy-viscosity turbulence models for engineering applications. AIAA J. 32 (8), 1598–1605.

Menter, F.R., 2009. Review of the shear-stress transport turbulence model experience from an industrial perspective. Int. J. Comput. Fluid Dyn. 23 (4), 305–316.

Prasad, A.K., 2000. Stereoscopic particle image velocimetry. Exp. Fluids 29, 103–116.

Raffel, M., Willert, C., Wereley, S., Kompenhans, J., 2007. Particle Image Velocimetry: A Practical Guide, 2nd edition. Springer-Verlag, Berlin-Heidelberg.

Reuther, J., Alonso, J.J., Vassberg, J., Jameson, A., Martinelli, L., 1997. An Efficient Multiblock Method for Aerodynamic Analysis and Design on Distributed Memory Systems. AIAA Paper 97-1893.

Rumsey, C.L., 2007. Apparent transition behavior of widely-used turbulence models. Int. J. Heat Fluid Flow 28 (6), 1460–1471.

Rumsey, C.L., Spalart, P.R., 2008. Turbulence model behavior in low Reynolds number regions of aerodynamic flowfields. In: The 38th AIAA Fluid Dynamics Conference and Exhibit, Seattle, Washington.

Scheurich, F., Brown, R.E., 2011. Effect of dynamic stall on aerodynamics of vertical axis wind turbines. AIAA J. 49 (11), 2511–2521.

Sheldahl, R.E., Klimas, P.C., 1981. Aerodynamic Characteristics of Seven Symmetrical Airfoil Sections Through 180-Degree Angle of Attack for Use in Aerodynamic Analysis of Vertical Axis Wind Turbines. Sandia National Laboratories Technical Report SAND-80-2114.

Sheng, J., Meng, H., Fox, R.O., 2000. A large eddy piv method for turbulence dissipation rate estimation. Chem. Eng. Sci. 55, 4423–4434.

Smagorinsky, J., 1963. General circulation experiments with the primitive equations. i. the basic experiment. Mon. Weather Rev. 91 (3), 99–164.

Soloff, S.M., Adrian, R.J., Liu, Z.-C., 1997. Distortion compensation for generalized stereoscopic particle image velocimetry. Meas. Sci. Technol. 8 (12), 1441–1454.

Soria, J., 1996. An investigation of the near wake of a circular cylinder using a video-based digital cross-correlation particle image velocimetry technique. Exp. Therm. Fluid Sci. 12 (2), 221–233.

Spalart, P.R., Allmaras, S.R., 1992. A one-equation turbulence model for aerodynamic flows. In: The 30th AIAA Aerospace Sciences Meeting and Exhibit, Reno NV. AIAA92-0439.

Spalart, P.R., Allmaras, S.R., 1994. A one-equation turbulence model for aero-dynamic flows. La Rech. Aerosp. 1, 5–21.

Srinivasan, G.R., Ekaterinaris, J.A., McCroskey, W.J., 1995. Evaluation of turbulence models for unsteady flows over an oscillating airfoil. Comput. Fluids 24 (7), 833–861.

Sutherland, H.J., Berg, D.E., Ashwill, T.D., 2012. A Retrospective of Vawt Technology. Sandia Report SAND 2012-0304.

van der Weide, E., Kalitzin, G., Schluter, J., Alonso, J.J., Unsteady Turbomachinery Computations Using Massively Parallel Platforms. AIAA Paper 421.

van Oudheusden, B.W., 2013. Piv-based pressure measurement. Meas. Sci. Technol. 24 (3), 032001.

Vinokur, M., 1983. On one-dimensional stretching functions for finite-difference calculations. J. Comput. Phys. 50 (2), 215–234.

Weiss, J.M., Smith, W.a., 1995. Preconditioning applied to variable and constant density flows. AIAA J. 33 (11), 2050–2057. http://dx.doi.org/10.2514/3.12946.

Westerweel, J., Scarano, F., 2005. Universal outlier detection for piv data. Exp. Fluids 39 (6), 1096–1100.

Whittlesey, R.W., Liska, S.C., Dabiri, J.O., 2010. Fish schooling as a basis for vertical-axis wind turbine farm design. Bioinspiration Biomim. 5, 1–6.

Wilcox, D.C., 1988. Reassessment of the scale-determining equation for advanced turbulence models. AIAA J. 26 (11), 1299–1310.

Wilcox, D.C., 1998. Turbulence Modeling for CFD, 2nd edition. DCW Industries, La Cañada, California.

Willert, C.E., Gharib, M., 1991. Digital particle image velocimetry. Exp. Fluids 10 (4), 181–193.

Yakhot, V., Orzag, S.A., 1986. Renormalization group analysis of turbulence. I—Basic theory. J. Sci. Comput. 1 (1), 3–51.